ACS APPLIED MATERIALS & INTERFACES

www.acsami.org

Research Article

Structural, Optical, and Electronic Properties of Cu-Doped TiN_xO_y Grown by Ammonothermal Atomic Layer Deposition

Filipp A. Baron,* Yurii L. Mikhlin, Maxim S. Molokeev, Mikhail V. Rautskiy, Ivan A. Tarasov, Mikhail N. Volochaev, Lev V. Shanidze, Anna V. Lukyanenko, Tatiana E. Smolyarova, Stepan O. Konovalov, Fyodor V. Zelenov, Anton S. Tarasov, and Nikita V. Volkov

Cite This: *ACS Appl. Mater. Interfaces* 2021, 13, 32531−32541

Read Online

ACCESS | Metrics & More | Article Recommendations

ABSTRACT: Copper-doped titanium oxynitride (TiN_xO_y) thin films were grown by atomic layer deposition (ALD) using the $TiCl_4$ precursor, NH_3, and O_2 at 420 °C. Forming gas was used to reduce the background oxygen concentration and to transfer the copper atoms in an ALD chamber prior to the growth initiation of Cu-doped TiN_xO_y. Such forming gas-mediated Cu-doping of TiN_xO_y films had a pronounced effect on their resistivity, which dropped from 484 ± 8 to 202 ± 4 μΩ cm, and also on the resistance temperature coefficient (TCR), which decreased from 1000 to 150 ppm °C^{-1}. We explored physical mechanisms causing this reduction by performing comparative analysis of atomic force microscopy, X-ray photoemission spectroscopy, X-ray diffraction, optical spectra, low-temperature transport, and Hall measurement data for the samples grown with and without forming gas doping. The difference in the oxygen concentration between the films did not exceed 6%. Copper segregated to the TiN_xO_y surface where its concentration reached 0.72%, but its penetration depth was less than 10 nm. Pronounced effects of the copper doping by forming gas included the TiN_xO_y film crystallite average size decrease from 57−59 to 32−34 nm, considerably finer surface granularity, electron concentration increase from 2.2(3) × 10^{22} to 3.5(1) × 10^{22} cm^{-3}, and the electron mobility improvement from 0.56(4) to 0.92(2) cm^2 V^{-1} s^{-1}. The DC resistivity versus temperature $R(T)$ measurements from 4.2 to 300 K showed a Cu-induced phase transition from a disordered to semimetallic state. The resistivity of Cu-doped TiN_xO_y films decreased with the temperature increase at low temperatures and reached the minimum near T = 50 K revealing signatures of the quantum interference effects similar to 2D Cu thin films, and then, semimetallic behavior was observed at higher temperatures. In TiN_xO_y films grown without forming gas, the resistivity decreased with the temperature increase as $R(T) = -1.88T^{0.6} + 604$ μΩ cm with no semimetallic behavior observed. The medium range resistivity and low TCR of Cu-doped TiN_xO_y make this material an attractive choice for improved matching resistors in RF analog circuits and Si complementary metal−oxide−semiconductor integrated circuits.

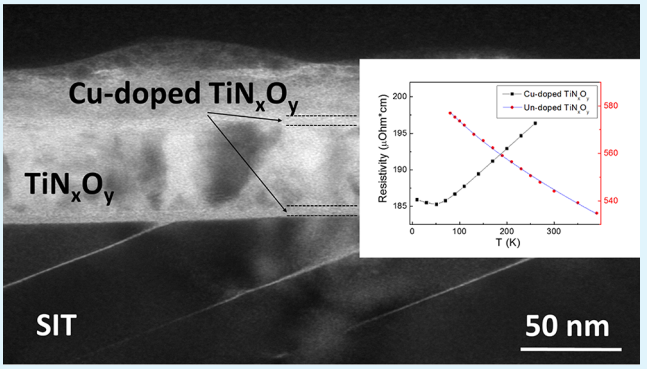

KEYWORDS: *atomic layer deposition, titanium oxynitride, copper doping, surface segregation, thin film*

INTRODUCTION

There is an increasing demand for TiN_xO_y thin films in various technology fields. Due to the persistent integration trend in wireless communications toward system-on-chip (SoC) solutions, some high-frequency circuits need integrated medium range thin film resistors (0.1−10 kΩ) with a small layout footprint and low-temperature coefficient of resistance (TCR).[1,2] TiN_xO_y is a potential material choice for such thin film resistors. The complementary metal−oxide−semiconductor (CMOS) industry typically uses a TiN barrier layer to prevent the copper diffusion from the metal routings in the back-end-of-the-line (BEOL) integrated circuit (IC) fabrication process.[3] Oxygen incorporation stuffs the TiN grain boundaries and improves the effectiveness of the diffusion barrier.[4] TiN_xO_y also prevents oxidation of the copper routings.[5] Other applications of TiN_xO_y films include low leakage MIM capacitors,[6] photocatalysts,[7,8] solar-selective absorbing coatings,[9,10] and the photovoltaic device power conversion efficiency boosters.[11] The addition of copper doping to TiN_xO_y should lower its resistivity and TCR,

Received: April 30, 2021
Accepted: June 17, 2021
Published: June 28, 2021

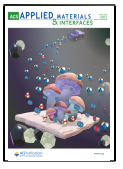

https://doi.org/10.1021/acsami.1c08036
ACS Appl. Mater. Interfaces 2021, 13, 32531−32541

improve its photocatalytic properties by decreasing the band gap energy, and make TiN_xO_y useful for medical applications as antibacterial coatings similar to Cu-doped TiO_2.[12−17] Although some work has been done on Cu-doped TiN and oxygen diffusion in Cu/TiN/Al, no in-depth experimental studies of Cu-doped TiN_xO_y films' physical properties have been published to the best of our knowledge.[18,19]

Magnetron sputtering,[2,20,21] reactive sputtering,[22−24] pulsed laser deposition,[25] and atomic layer deposition (ALD) are the major technologies to produce TiN_xO_y thin films as they do not require elevated temperatures while providing good conformity.[6,26,27] The self-limiting nature of the ALD growth and the ability to grow on the shaded and even upside-down surfaces make this technology more favorable for certain applications.[28−30] ALD provides unsurpassed accuracy of the film thickness and uniformity; therefore, we believe that this technology is a highly promising route to develop TiN_xO_y resistors for high-frequency integrated circuits in the future. However, compared to magnetron sputtering, ALD usually does not have high vacuum, which may result in a less precisely defined oxygen content in TiN_xO_y films due to the admixture of residual oxygen in the ALD chamber during the growth. Thus, one may have increased TiN_xO_y resistivity spread across the wafer that would result in reduced manufacturing yield of TiN_xO_y resistors. We explored the possibility of TiN_xO_y film resistivity reduction and stabilization by copper doping of the films during their growth in the presence of loosely defined oxygen concentration in the ALD chamber. In addition, our analysis provides a glimpse on how the copper atoms distribute across the TiN_xO_y layer and allows one to determine their effective penetration depth. The focus of this paper is on the comparative study of structural, optical, and electronic properties of the TiN_xO_y thin films grown with and without forming gas-mediated copper doping. We performed TiN_xO_y film ALD growth and characterization and conducted their physical property study using DC resistivity and Hall measurements, TEM, AFM, XRD, XPS, and optical spectral ellipsometry analyses.

EXPERIMENTAL SECTION

TiN_xO_y Sample Fabrication. Titanium oxynitride films were grown by thermal ALD in a Picosun SUNALE R-200 ADVANCED reactor without load lock. The wafers used for the film growth were a mirror-finished CT-32-1 Sitall (SIT), which is a Mg-doped quartz-like polycrystalline ceramic, sapphire, and atomic flat high resistivity 10 kΩ cm (100) silicon. The wafers were RCA1 and DI water-cleaned, dried in 5 N pure nitrogen, and then placed in a basket and manually loaded into an ALD reactor installed in Class 1000 clean rooms. The chamber was flushed with 8 N pure nitrogen five times and then annealed at 420 °C for 4 h. A TiN growth recipe was used, in which the $TiCl_4$ precursor (5 N pure) and NH_3 (6 N pure) ammonia gas were sequentially pulsed for 0.1 and 1 s at each growth cycle. $TiCl_4$ pulses were purged with nitrogen (7 N pure) at a 150 sccm flow rate for 2 s, while NH_3 was purged at 100 sccm for 4 s. The maximum pressures of $TiCl_4$ and NH_3 pulses reached 25−30 and 40−45 hPa accordingly. The base pressure was 5−7 hPa, and the intermediate space nitrogen flow (IMS) was 200 sccm. TiN_xO_y film growth proceeded due to the incorporation of the chamber residual oxygen. Prior to the TiN_xO_y film growth of actual samples, the reactor chamber was passivated by 2000 growth cycles of TiN_xO_y at 420 °C. The forming gas used was a mixture of 3% of hydrogen (6 N pure) in nitrogen (5 N pure) supplied into the ALD chamber by 15 s pulses for 15 min without a nitrogen purge.

Transmission Electron Microscopy (TEM). The cross-sectional TEM specimens were prepared by a focused ion single-beam system (FIB) Hitachi FB-2100 (40 keV Ga+). A Ge protective layer was deposited before specimen preparation. The Ge layer was necessary to protect the film from structural degradation during FIB preparation (tungsten mask deposition and sputtering). TEM images were acquired with a Hitachi HT7700 microscope operating at 100 kV and an emission current of 8 μA.

Atomic Force Microscopy (AFM). The film surface morphology was studied by AFM with the surface feature size distributions obtained by statistical analysis. We used a NanoInk DPN 5000 with a silicon cantilever with a tip radius <10 nm (part number CSG01 from TipsNano) in constant force full contact mode. The readout was processed by the Gwyddion v.2.51 and ImageJ software.

X-ray Photoelectron Spectroscopy (XPS). The film chemical composition was determined using the X-ray photoelectron spectra collected using a SPECS instrument equipped with a PHOIBOS 150 MCD 9 hemispherical analyzer at pass energies of 20 eV for survey spectra and 10 eV for high-resolution spectra. Monochromatic Al *Kα* radiation (1486.6 eV) was used for excitation of the spectra presented here. Relative concentrations of elements were determined from the survey spectra using empirical sensitivity coefficients. The high-resolution spectra were fitted with Gaussian−Lorentzian peak profiles after Shirley background subtraction with CasaXPS software. The surface of the samples was somewhat contaminated with carbon, and the oxygen content was higher than nitrogen. The XPS depth profile was obtained using Ar-ion sputtering (an energy of 2.5 keV and a beam current of 20 μA) of the TiN_xO_y film with an average etching rate of 2.75 Å min^{-1}. The average rate was determined by measuring the total TiN_xO_y thickness etching time with the process end detected by registering the first events of Mg and Si spectra coming from the sample SIT substrate.

X-ray Diffraction (XRD). The powder diffraction data of all samples for Rietveld analysis were collected at room temperature with a Bruker D8 ADVANCE powder diffractometer (Cu *Kα* radiation) and linear VANTEC detector. The step size of 2θ was 0.016°, and the counting time was 2 s per step.

Optical Spectral Ellipsometry. Optical properties were studied by ellipsometric measurements performed using a variable spectroscopic ellipsometer ELLIPS-1801 at T = 296 K following the experimental procedure described elsewhere.[31] The extraction was done according to a simple optical model of one solid isotropic layer on a substrate through the fitting procedure with the Forouhi−Bloomer dispersion formula.[32] The optical transmittance spectrum was calculated using the absorption coefficient extracted for the TiN_xO_y films with the account of internal transmission only. The optical characteristics of the substrate material used in the optical modeling were determined by measurements of the ellipsometric spectra of bare Si and SIT wafers. The thickness of the TiN_xO_y film was set as known a priori from TEM data.

Electrical Transport Measurements. The sheet resistance (R_s) of TiN_xO_y films was measured using standard four-point probe DC measurements. We checked the R_s uniformity across the samples and the growth-to-growth variation between different ALD runs by measuring each 60 × 48 mm^2 sample sheet resistance at nine points: one in the middle and eight points along the sample periphery. Hall measurements were carried out using the Van der Pauw method.[33] EPO-TEK H20E silver epoxy was used to connect the external wiring to the 10 × 10 mm^2 samples. A SourceMeter Keithley 2400 sent the current into the film, and a Nanovoltmeter Keithley 2182A sensed the Hall voltage in the external magnetic field swept from −900 to +900 mT. The current-reversal method was used to subtract the thermoelectric component from the Hall voltage. The source current for the resistivity measurements was 100 μA, and for the Hall voltage measurements, it was 1 mA. In the variable temperature resistivity and Hall measurements, the temperature was swept from low to high by quasi-static warm up.

RESULTS AND DISCUSSION

The presence of trace amounts of oxygen in the ALD chamber resulted in TiN_xO_y growth by a recipe originally designed for

https://doi.org/10.1021/acsami.1c08036
ACS Appl. Mater. Interfaces 2021, 13, 32531−32541

TiN. We used the forming gas-mediated copper doping (FGCD) of the ALD chamber and the wafers at 420 °C for 15 min followed by incorporation of the chamber-desorbed Cu atoms into the TiN_xO_y films during their growth. The actual film growth took place without the forming gas. There were two groups of samples grown: G1, unintentionally doped (hereafter referred to as "Un-doped") TiN_xO_y grown without forming gas ALD chamber pre-treatment, and G2, intentionally doped (Cu-doped) TiN_xO_y films grown with 300 pulses of FGCD prior to executing 2000 ALD growth cycles of the TiN recipe. Upon TiN_xO_y film growth completion, the chamber was nitrogen-vented; the samples were extracted and placed on a cold brick. To obtain Un-doped samples, the ALD chamber was passivated with 100−120 nm Al_2O_3 at 250 °C before wafer insertion and no FGCD was applied prior to the TiN_xO_y film growth initiation. Thus, the only difference in processing of Un-doped samples of the group G1 and Cu-doped samples of the group G2 is that, prior to the growth of G2, the ALD chamber has been treated with the forming gas carrying copper atoms. All TiN_xO_y samples appeared dark greenish gray and had a glossy metallic reflective surface, as shown in Figure 1. The samples grown without FGCD were slightly more grayish and less greenish than those grown using the FGCD process.

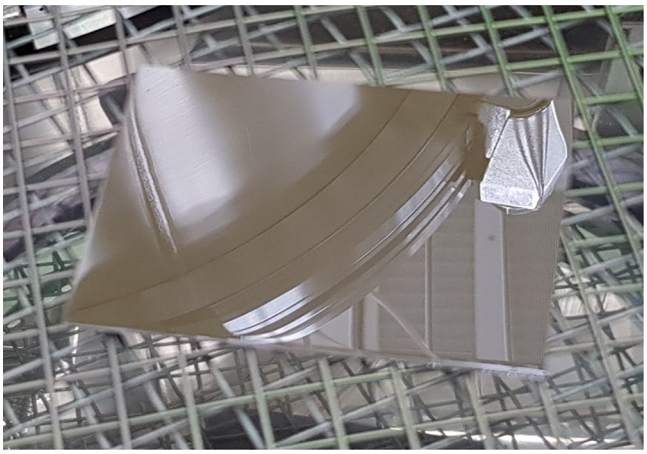

Figure 1. Cu-doped TiN_xO_y thin film sample grown on the CT-32-1 Sitall substrate at 420 °C by the ammonothermal atomic layer deposition of $TiCl_4$ in the presence of trace amounts of oxygen in the ALD chamber.

The overall effect of FGCD was a substantial reduction of the TiN_xO_y film sheet resistance (R_s) from 220 to 43 Ω □$^{-1}$ and its significant growth-to-growth variation reduction from >500% for Un-doped films to <15% for Cu-doped samples. Resistance measurement results for TiN_xO_y grown on SIT and sapphire are listed in Table 1. The relatively large variation of R_s in Cu-doped TiN_xO_y films was due to the resistance gradient along the G2 samples caused either by forming gas or residual oxygen directional flow inside the reactor. The second noticeable effect of FGCD was a 2-fold increase in the film growth rate per cycle (GPC), possibly due to residual chamber oxygen reduction by the forming gas annealing or the copper catalytic action. From the TEM image, we extracted the film thickness and found that the GPC for the G1 samples was 0.11 Å cycle^{-1}, which was significantly lower than 0.235 Å cycle^{-1} for the FGCD-treated (Cu-doped) G2 samples. The latter value is consistent with a GPC of 0.2−0.3 Å cycle^{-1} reported for undoped TiN_xO_y by others.[6,34−36]

Table 1. Summary of the Sheet Resistance Four-Point Probe Measurements of ALD-Grown TiN_xO_y Films with/without Copper Doping by the FGCD Process

	Un-doped TiN_xO_y	Cu-doped TiN_xO_y
R_s at the wafer center (Ω □$^{-1}$)	224	49
mean R_s (Ω □$^{-1}$)	220	43
R_s variation (%)	8	15
growth-to-growth R_s variation (%)	>500	<15

To calculate the resistivity of the TiN_xO_y films, we extracted their thickness from corresponding TEM cross-sectional images. Shown in Figure 2 is the TEM cross section of

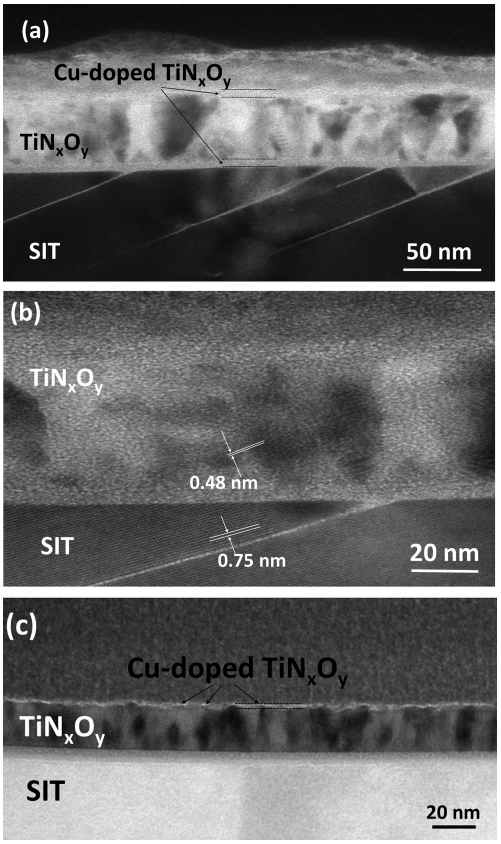

Figure 2. TEM images of Cu-doped TiN_xO_y films grown on the SIT wafer by 420 °C ammonothermal ALD in the presence of background oxygen by the FGCD process: (a) the copper surface segregation layer and V-shaped nanocrystallites are clearly visible, (b) interplanar spacing of TiN_xO_y nanocrystallites and SIT, and (c) the unintentionally doped TiN_xO_y film (grown without the FGCD process), which shows a residual thin layer of segregated Cu impurities on the surface due to the chamber background Cu-doping.

TiN_xO_y/SIT films with and without FGCD. All samples inspected showed uniform layers of TiN_xO_y with thicknesses of 22 ± 1 nm for G1 and 47 ± 1 nm for G2 films. Based on the sheet resistance measurements and the film thickness extracted from TEM, the TiN_xO_y effective resistivity was calculated: 484 ± 8 μΩ cm for G1 and 202 ± 4 μΩ cm for G2 samples, so the FGCD process decreased the TiN_xO_y resistivity more than twice. The resistivity of the FGCD-treated films was close to average values reported for ALD-grown TiN: 70−300 μΩ cm.[26,37−39] Therefore, our result appeared surprisingly low as

https://doi.org/10.1021/acsami.1c08036
ACS Appl. Mater. Interfaces 2021, 13, 32531−32541

the films were grown using the ALD reactor without load lock with a considerable amount of residual oxygen, so the O-content and resistivity of thus obtained TiN_xO_y films were supposed to be large. TEM also revealed V-shaped nanocrystallites of TiN_xO_y embedded in the amorphous TiN_xO_y film of the G2 samples, and similar features have been reported by others.[40] The measured interplanar spacing values are 4.8 Å for TiN_xO_y nanocrystallites and 7.5 Å for SIT.

The surface morphology of the Un-doped and Cu-doped TiN_xO_y films obtained by AFM was notably different (Table 2). Statistical analysis of the AFM data collected from the 5 × 5 μm^2 area revealed the surface RMS and maximum peak-to-peak values of 7.95 and 63.4 nm for the Un-doped G1 sample and 5.16 and 46.1 nm for the Cu-doped G2. The grains of G1 were significantly wider (133−196 nm) than those of G2 (9.78−10.9 nm). The Cu-doped samples were notably smoother, namely, a 50% smaller average surface roughness, 30% smaller grain maximum height, and 1 order of magnitude narrower grain horizontal size distribution. RMS values from other reports are 14.64 and 8.21 Å for TiN_xO_y grown at 350 and 500 °C, respectively,[37] and 3.14,[39] 2.58,[41] and 9−15 Å.[42] The SIT wafers used for growth had a 10−15 nm average roughness created by ∼100 nm wide grains, which affected the RMS statistics for both G1 and G2 films. To subtract the rough substrate effect, we reduced the scan window to 500 × 500 nm^2 to avoid the SIT grain capture and obtained the following values: G1 sample: S_q = 2.63 nm, S_a = 1.93 nm; G2 sample: S_q = 1.58 nm, S_a = 1.27 nm, which were still higher but much closer to other reports. The surface morphology difference between G1 and G2 films seems consistent with their resistivity trend, so the surface scattering mechanism might be one of the mobility limiting processes present in both samples at different rates.

Another differentiating factor between G1 and G2 samples was their chemical composition, as revealed by the XPS spectra shown in Figure 3. The comparative analysis revealed a prevailing fraction of oxygen in both G1 and G2 samples (Table 3). Based on the surface spectra, the effective stoichiometric formulae read $TiN_{0.82}O_{1.43}$ (or $Ti_{31}N_{25}O_{44}$) for G1 and $TiN_{0.87}O_{1.35}$ (or $Ti_{31}N_{27}O_{42}$) for G2 films. The surface spectra of Cu-doped TiN_xO_y showed a few percent lower oxygen concentration, higher nitrogen content, smaller share of the transitional TiN_xO_y phase (binding energy Ti $2p_{3/2}$ of 456.7 eV), more of TiN (455.2 eV), and a higher content of TiO_2 (458.5 ɜB) than Un-doped films. Compared to the TiN_xO_y film grown from the TDMAT precursor, forming gas, and oxygen remote plasma ALD, we have a substantially larger share of transitional TiN_xO_y than the TiN phase with the 461 eV TiN peak completely missing.[11] Also shown in Figure 3 are the nitrogen (N 1s: N−Ti = 396.9 eV, N−TiO = 396.2 eV, and N−O or N−C = 401.6 eV) and oxygen (O 1s: O−Ti = 529.9 eV, O−TiN = 531.5 eV, and O−C or O−N = 533.0 eV) XPS peaks. The binding energies obtained were in good agreement with other works[22,43−48] but one.[42]

The XPS depth profiles of the Ti-, N-, and O-contents (Figure 4) revealed that the surface composition was slightly different from the deep layers of TiN_xO_y in both G1 and G2 samples. The difference in the oxygen concentration between G1 and G2 samples did not exceed 6% and was localized within 8 nm from the film surface. The reduced oxygen concentration in G2 along with its smoother surface measured by AFM was consistent with others.[19] Deeper layers of TiN_xO_y had almost the same N/O-content in both Un-doped/Cu-doped samples and increased Ti-share relative to the surface, resulting in the effective formula $TiN_{0.74}O_{1.06}$ (or $Ti_{36}N_{27}O_{38}$). Notable carbon surface contamination was found, but its content dropped within a few nanometers under the surface, and it was strongly correlated with the titanium content abrupt increase by 7%. Another observation was that Un-doped films contained some chlorine (<0.5%) contamination from decomposed $TiCl_4$ precursor residuals, while the G2 sample showed only traces of chlorine (<0.1%). The chlorine and copper content, although small, did not decay as quickly as

Table 2. Sample AFM Surface Morphology Analysis of the TiN_xO_y Films Grown on SIT: (Left Columns) Un-Doped and (Right Columns) with Cu-Doping[a]

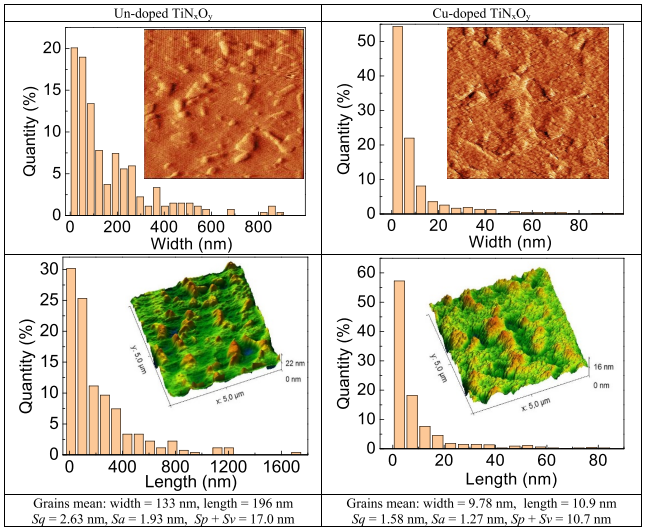

[a]The histograms were extracted from AFM data and represent the grain horizontal (upper row) width and (lower row) length distribution over the scanned 5 × 5 μm^2 area. The insets show the sample 2D/3D surface scans.

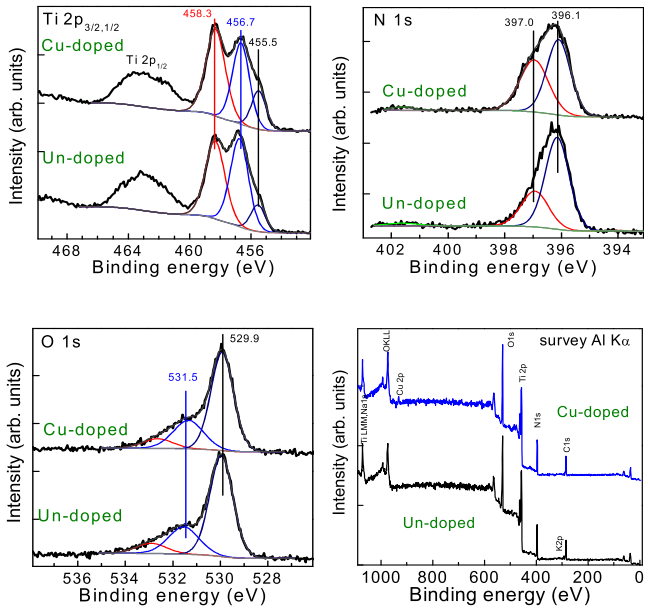

Figure 3. XPS data for TiN_xO_y/SIT films grown by ALD with and without copper doping by the FGCD process.

https://doi.org/10.1021/acsami.1c08036
ACS Appl. Mater. Interfaces 2021, 13, 32531−32541

Table 3. TiN_xO_y/SIT Film Surface Composition and Binding Energies Extracted from the XPS Data

	Ti 2p		N 1s		O 1s		C	Cu	Cl
sample	at %	eV	at %	eV	at %	eV	at %	at %	at %
G1 Un-doped	23.9	455.5 (11)	19.6	396.2 (68)	34.2	529.9 (67)	21.7	0.28	0.3
		456.7 (46)		396.9 (30)		531.5 (24)			
		458.3 (43)		401.6 (2.5)		533.0 (9)			
G2 Cu-doped	24.3	455.5 (16)	21.1	396.1 (53)	32.7	529.9 (66)	20.8	0.72	<0.1
		456.7 (38)		397.0 (45)		531.3 (25)			
		458.3 (46)		401.6 (2)		533.0 (9)			

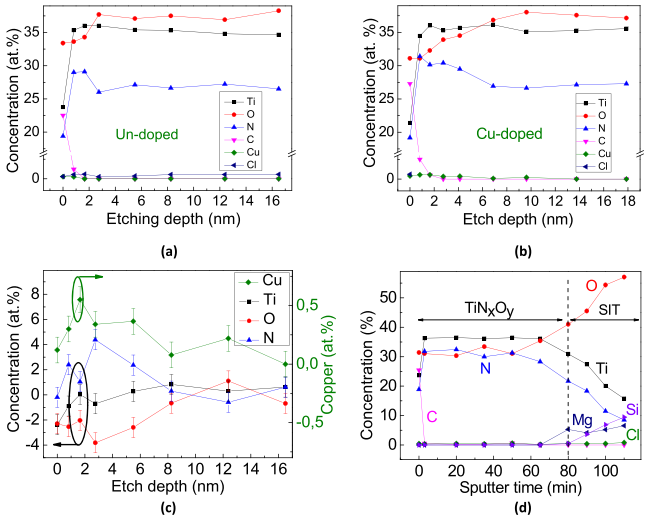

Figure 4. XPS depth profile of the TiN_xO_y/SIT films grown by ALD (a) Un-doped (G1) and (b) Cu-doped (G2), (c) the element concentration difference between G2 and G1 samples (G2−G1), and (d) concentration profile versus the sputter time.

carbon. We believe that they were incorporated during the film growth in the ALD chamber followed by surface segregation, which is why we observe them at both the surface and the TiN_xO_y/SIT interface. Missing satellites near Cu 2p at 944−946 eV in the XPS spectrum were interpreted as the signature of metallic non 2^+-valent copper, so we believe that TiN_xO_y films were interstitially Cu-doped. G2 samples had about 0.72%, while G1 contained 0.28% of copper at the TiN_xO_y surface. So, in fact, the G1 samples were also slightly Cu-doped but at a considerably lower (close to the detection limit) level and much faster decrease with depth than in G2 films, which is consistent with a much thinner layer of copper impurities visible on the TEM image of G1. Therefore, for mere convenience, throughout this report, we use the term "Un-doped" as a shorthand for "unintentionally background induced low level copper doping of samples grown without FGCD" and we do not claim that G1 samples were completely free of Cu-doping. This unintentional Cu-doping of G1 was apparently due to the residual Cu atoms diffusing through the protective Al_2O_3 chamber passivation layer at 420°. The relative excess of nitrogen and depletion of oxygen near the surface of G2 samples coincide with the copper localization region. These data are consistent with the TEM image showing different texture Cu-rich regions near the surface and the TiN_xO_y/SIT interface of the G2 sample. The copper doping could act as a Ti-nitration catalyst and Ti-oxidation inhibitor, thus increasing the N/O ratio wherever present and boosting the overall growth rate of the TiN_xO_y film. Its shallow diffusion into TiN_xO_y has been attributed to the oxygen-stuffed TiN grain boundaries.[19]

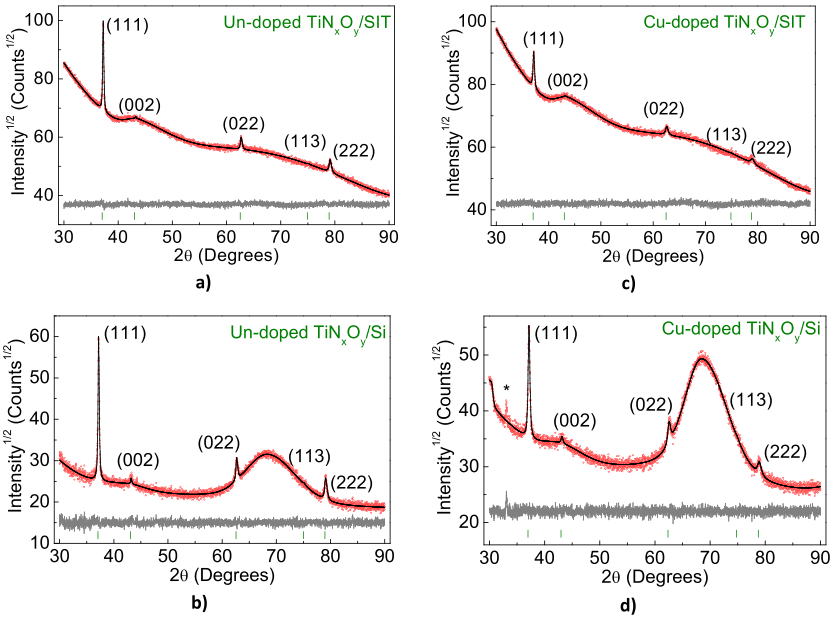

Figure 5. Difference Rietveld plots of the ALD TiN_xO_y films grown: (a) Un-doped on Sitall (G1/SIT), (b) Un-doped on silicon (G1/Si), (c) Cu-doped on Sitall (G2/SIT), and (d) Cu-doped on silicon (G2/Si); the unindexed impurity peak is marked by an asterisk.

https://doi.org/10.1021/acsami.1c08036
ACS Appl. Mater. Interfaces 2021, 13, 32531−32541

Table 4. Main Parameters of the XRD Processing and Refinement of the TiN_xO_y Samples G1 and G2 Grown on Si and SIT Substrates[a]

	Un-doped G1/SIT	Un-doped G1/Si	Cu-doped G2/SIT	Cu-doped G2/Si
a (Å)	4.1981(6)	4.1957(5)	4.2027(18)	4.2072(14)
V (Å^3)	73.99(3)	73.86(3)	74.23(10)	74.47(7)
Ti−Ni (Å)	2.0991(3)	2.0979(3)	2.1014(9)	2.1036(7)
R_{wp} (%)	1.78	4.55	1.61	3.16
R_p (%)	1.40	3.56	1.27	2.45
R_{exp} (%)	1.69	4.02	1.48	2.84
χ^2	1.05	1.13	1.09	1.11
R_B (%)	0.17	0.33	0.27	0.18
average crystallite size (nm)	59(2)	57(2)	34(2)	32(1)

[a]Space group, *Fm*-3*m*, Z = 4, 2θ-interval = 30−90°. Summarized here are the extracted lattice parameters of the TiN_xO_y films, main Ti−Ni bond length (symmetry code: (i) $x - 1/2$, $y - 1/2$, z), *R*-factors, and isotropic displacement for Ti and N.

To explore whether the drastic difference between the G1 and G2 film resistivities could be due to the TiN_xO_y film phase/stoichiometry difference, we conducted their XRD analysis. One needed to be cautious about the substrate interference with the X-ray signal from the thin film. To distinguish between the substrate and film response, we performed XRD analysis of two pairs of G1 and G2 samples: one sample of each group grown on SIT and on silicon wafer (see Figure 5). All peaks, besides one small impurity peak in G2/Si (Figure 5d), were indexed by a cubic cell (*Fm*-3*m*) with parameters close to TiN_xO_y.[49] Therefore, this structure served as the starting model for the Rietveld refinement procedure using TOPAS 4.2 guidelines.[50] All models included intensity correction due to the preferred orientation on the (111) plane. Refinements were stable and yielded low *R*-factors. Table 4 summarizes the XRD results.

The XRD analysis of the crystal structure revealed that G1/SIT and G1/Si samples had similar cell volumes in the narrow range of 73.86−73.99 Å^3. The G2/SIT and G2/Si samples also had similar cell volumes in the range of 74.23−74.47 Å^3, but these values were appreciably larger than those for the G1 samples (Table 4), which confirmed that G1 and G2 samples had slightly different chemical compositions. It should be noted that G1 and G2 samples had cell volumes much smaller than the cell volume of pure TiN V = 76.4 Å^3.[49] Since the O^{2-} ion has a smaller ion radius IR(O^{2-}, CN = 6) = 1.4 Å than the N^{3-} ion IR(N^{3-}, CN = 6) = 1.54 Å, one may conclude that G1 and G2 samples have O^{2-}-doping. We believe that O^{2-}-doping was substituting nitrogen because interstitial O^{2-}-doping would result in the cell volume increase, which was not observed.

The G1 sample cell volume was smaller, indicating a higher O-content than in G2, in accord with the XPS results. Based on the data previously reported by others, the 36.95, 42.95, and 62.25° peaks correspond to the (111), (002), and (022) TiN phases, while the 74.78 and 78.9° peaks are the (113) and (222) TiN phases, respectively.[37,51] Using the XRD peak full width at half-maximum and subtracting the background signal according to TOPAS 4.2 guidelines, we calculated the average TiN_xO_y crystallite sizes to be 59(2) nm in Un-doped TiN_xO_y/SIT, 34(2) nm in Cu-doped TiN_xO_y/SIT, 57(2) nm in Un-doped TiN_xO_y/Si, and 32(1) nm in Cu-doped TiN_xO_y/Si. This is in qualitative agreement with our AFM results confirming finer granularity of Cu-doped TiN_xO_y films.

The optical characteristics of titanium oxynitride thin films vary significantly as multiple factors may affect them, of which the substrate and interface quality are usually the most pronounced.[22,25,52] Indeed, the surface morphology and processing quality may result in a significant shift of the transmittance band even in pure TiN samples.[21,53,54] Spectral ellipsometry of our samples confirms that the substrate type strongly affects the optical response of the TiN_xO_y films. The films grown on Si showed a higher refractive index and slightly lower absorption coefficient than those on SIT. Figure 6a shows that the Cu-doping effect on the film refraction index was in the opposite direction for films grown on Si and SIT. Cu-doped samples showed a much narrower difference between their indices, which coincided completely at 500−600 nm wavelengths, demonstrating the film properties' stabilizing effect of the copper doping. The refraction index of Cu-doped films at 633 nm was about 25% lower than that reported in the literature for the same O-content undoped TiN_xO_y films grown by ALD.[6] At a 500 nm wavelength, both the refraction index and absorption coefficient of our samples (except for undoped TiN_xO_y/SIT) matched the values measured in sputtered TiN_xO_y films.[55] Figure 6b shows that

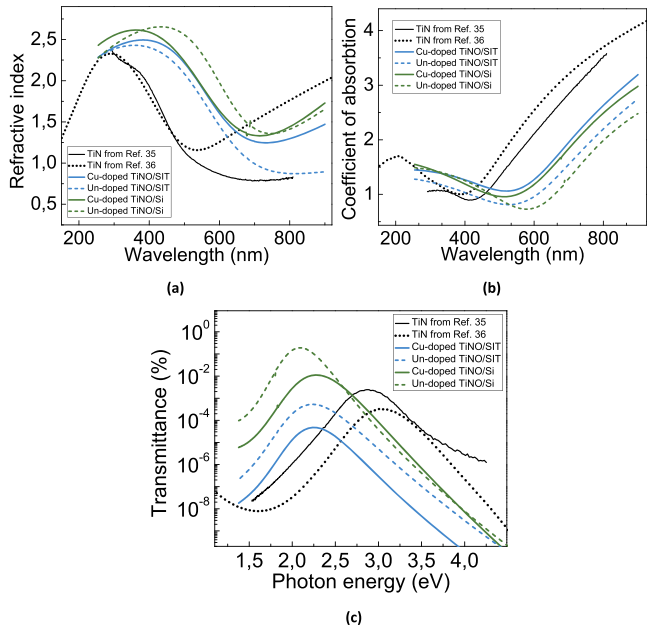

Figure 6. Plots of the (a) refraction index, (b) coefficient of absorption, and (c) transmittance of the ALD Cu-doped/Un-doped TiN_xO_y films grown on SIT and Si wafers obtained by optical ellipsometry.

https://doi.org/10.1021/acsami.1c08036
ACS Appl. Mater. Interfaces 2021, 13, 32531−32541

the FGCD process caused a 30−50% increase in the TiN_xO_y film absorption coefficient and an ∼50 nm blue shift in all films grown on both Si and SIT. From the literature available on this topic, it follows that those TiN_xO_y thin films with an oxygen concentration below 40 at % are strongly absorbing in the visible and near-infrared range.[55,56] However, despite clear resemblance of the transmittance spectra shown in Figure 6c to those published in the literature, our transmittance magnitudes are smaller than the values reported for similar composition sputtered films highlighting the enhanced metallic properties of our samples.[55,56] Indeed, our data look more like 0.5−1 eV red-shifted spectra of pure TiN.[53,54]

The later phenomenon also manifests itself in the red shift of zero crossing of the real part of dielectric permittivity of our TiN_xO_y samples (Figure 7) compared to Un-doped TiN_xO_y.[22]

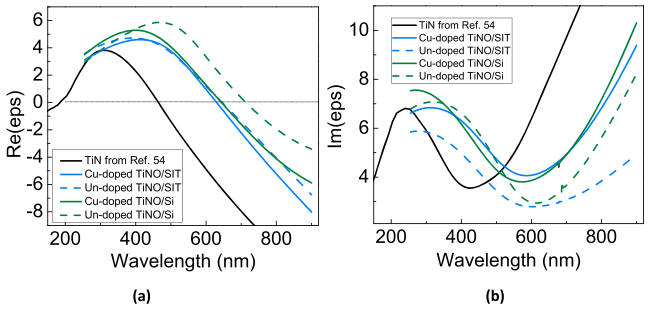

Figure 7. Optical spectra for (a) real and (b) imaginary parts of the dielectric permittivity of Cu-doped/Un-doped TiN_xO_y films grown on SIT and Si wafers.

On the other hand, based on the XPS data of G1 and G2 samples, the oxygen concentration difference between the samples did not exceed 6% near the surface and 1% in the bulk. We believe that it is hard to account for large (up to 10 times) transmittance differences and the curves' significant blue shift (Figure 6c) on the basis of the O-content variation only. Thus, we believe that the optical spectral ellipsometry data indicate a significant role of copper doping in enhanced metallic properties of our samples. We carried out the DC electronic transport measurements to quantify those properties.

The Hall measurements revealed n-type conductivity in all samples. Table 5 summarizes our results calculated based on

Table 5. Results of Hall Measurements of TiN_xO_y Films Grown on SIT Wafers

	Un-doped TiN_xO_y	Cu-doped TiN_xO_y
film thickness (nm)	22 ± 1	47 ± 1
resistivity ($\mu\Omega$ cm)	519 ± 10	198 ± 5
Hall constant R_H ($cm^3\ C^{-1}$)	$-2.9(2) \times 10^{-4}$	$-1.81(6) \times 10^{-4}$
carrier concentration (cm^{-3})	$2.2(3) \times 10^{22}$	$3.5(1) \times 10^{22}$
carrier mobility ($cm^2\ V^{-1}\ s^{-1}$)	0.56(4)	0.92(2)

the film thicknesses extracted from TEM data. The electron concentration extracted from the Hall measurements of G1 and G2 samples was consistent with the optical measurement results revealing enhanced carrier concentration in the G2 sample. The electron mobility and concentration were approaching the values reported for pure TiN.[57−60]

We also explored the low-temperature behavior of resistivity, free carrier concentration, and mobility and did temperature-dependent Hall measurements of Cu-doped TiN_xO_y samples. Results are shown in Figure 8. No sensitivity to light and a magnetic field of up to 1 T have been found. Higher fields/

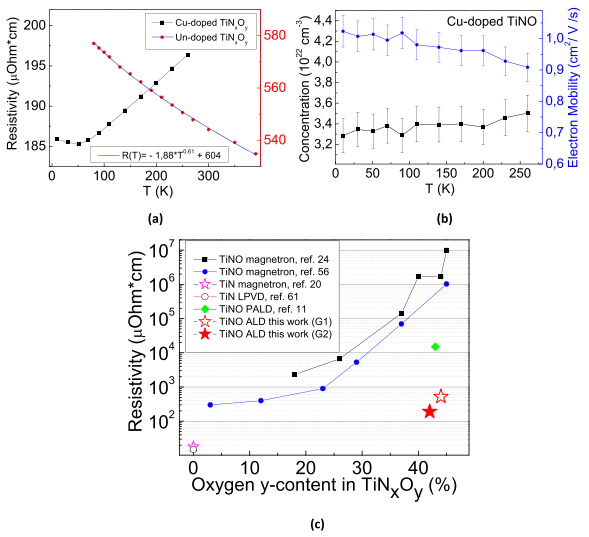

Figure 8. Measurement results: (a) resistivity versus temperature in TiN_xO_y/SIT films, (b) electron concentration/mobility versus temperature in Cu-doped TiN_xO_y/SIT films extracted from the Hall effect measurements, and (c) room-temperature resistivity versus the oxygen y-content in TiN_xO_y films grown by different groups.

accuracy measurements are planned in the future. The resistivity temperature dependence $R(T)$ in the range of 4.2−300 K (Figure 8a) for the G2 films followed the behavior of single-crystal TiN but showed considerably smaller variation. Figure 8b shows almost flat electron concentration and effective mobility versus temperature in the Cu-doped films. Indeed, the resistivity variation of Cu-doped TiN_xO_y was less than 5% compared to almost 90% for monocrystalline TiN.[20,61] At the same time, the effective resistivity of Cu-doped TiN_xO_y is higher than in pure TiN. Our $R(T)$ data for the G2 sample show a resistivity minimum at 50 K, and the curve shape is quite similar to the pulsed laser-deposited (PLD) single-crystalline TiN by Roy et al., but the absolute values are 30% smaller.[62] The low-temperature negative TCR may originate from the electron−electron interaction,[63] hopping conduction,[40] or 2D weak localization phenomena.[64] The onset of positive TCR at temperatures above 50 K may be either due to electron−phonon or charged-impurity scattering processes.[63,65] The positive TCR branch was completely missing in Un-doped G1 samples (Figure 8a), which showed a strictly negative TCR at all temperatures best fitted by the relationship $R(T) = -1.88T^{0.6} + 604\ \mu\Omega$ cm. Such behavior is a signature of the electron−electron (e−e) interaction or weak scattering on disordered fixed defects that follow a similar law $R(T) \approx aT^{0.5}$, and coefficient a is known to change sign as a function of disorder.[62,63] It is quite different from both moderately doped semiconductors where scattering is dominated by ionized impurities $R(T) \approx T^{-1.5}$ and heavily doped semiconductors, which have positive TCR at low temperatures.[66,67]

Figure 8c summarizes the data for resistivity dependence on the oxygen y-content in TiN_xO_y films grown by different researchers.[11,20,24,55,61] The resistivity of our ALD grown Cu-doped TiN_xO_y films was 10−20 times higher than those of the magnetron-sputtered and laser physical vapor-deposited

https://doi.org/10.1021/acsami.1c08036
ACS Appl. Mater. Interfaces 2021, 13, 32531−32541

(LPVD) monocrystalline TiN films.[20,61] However, it is over 3 orders of magnitude smaller than the values reported for similar composition-undoped TiN_xO_y films grown by DC magnetron sputtering.[24,55] These data along with the optical measurement results consistently point out at the copper doping dominating the transport properties in G2.

The role of oxygen receding from the surface in favor of copper may be also detrimental for the phase transition of $R(T)$ observed as the conductivity is very sensitive to the local O-content in TiN_xO_y near the percolation point.[6] Therefore, we conclude that the relatively low resistivity and high electron mobility in our samples (given the high O-content) are due to the surface-segregated copper doping and near-surface oxygen depletion. Assuming that the resistivity of undoped deeper layers of TiN_xO_y of G2 samples is the same as in G1 and the effective resistivity of G2 is known from measurements, one could estimate the effective resistivity of the Cu-doped near the surface layer by assuming the two-parallel resistor model. This model consists of an 8 nm-thick Cu-doped TiN_xO_y resistor and 39 nm-thick Un-doped TiN_xO_y resistor (484 $\mu\Omega$ cm) connected in parallel, which are equal to one 47 nm-thick resistor (202 $\mu\Omega$ cm). This model yields the effective resistivity of the Cu-doped TiN_xO_y thin surface layer equal to 52.6 $\mu\Omega$ cm, i.e., only 3 times higher than that of the single-crystal TiN. Detailed studies of the low-temperature transport physical (carriers scattering) mechanisms are under way, and they are beyond the scope of this paper.

In observance of the close similarity of the TiN_xO_y fabrication technology to the standard BEOL damascene process of forming Cu multilevel routing in integrated circuits for CPU and memory chips, the process integration of Cu-doped TiN_xO_y thin films should be realistic.[68,69] At the same time, this new material offers notable performance improvement over TiN for both the diffusion barrier and RF resistor applications.

CONCLUSIONS

Uniform TiN_xO_y thin films with stable physical properties have been grown by ammonothermal ALD at 420 °C in the presence of residual oxygen. The effect of the forming gas-mediated copper doping of the ALD chamber at 420 °C on the TiN_xO_y properties has been explored. The structural and physical properties of the films have been studied by AFM, TEM, XPS, XRD, optical reflectance spectroscopy, DC resistivity, and Hall measurements. We found that the intentional copper doping reduced the films' surface roughness and resistivity by 50%. Based on the XPS data, the surface-effective composition of the films was $TiN_{0.82}O_{1.43}$ for Un-doped and $TiN_{0.87}O_{1.35}$ for Cu-doped films, while the deep layers of both types had roughly the same composition of $TiN_{0.74}O_{1.06}$. Copper doping resulted in an almost 2-fold increase in the ALD growth rate, during which copper segregated to the surface where its concentration reached 0.72% but it dropped below the detection limit within 8−10 nm from the surface. We confirmed the enhanced Cu diffusion blocking capabilities of TiN_xO_y with an effective diffusion blocking range below 10 nm due to the oxygen-stuffed grain boundaries. XRD structural analysis revealed a 0.1% increase in the cell size and a 2-fold decrease in the average nanocrystallite size in the Cu-doped TiN_xO_y films.

The optical properties of Cu-doped TiN_xO_y films resembled those of TiN with a 0.5−1 eV red shift and differed from those of undoped TiN_xO_y with a similar O-content reported by others. Hall measurements revealed that Cu-doping resulted in a 50% increase in the effective electron concentration: 3.5×10^{22} cm^{-3} in G2 versus 2.2×10^{22} cm^{-3} in G1 samples and almost doubled the effective mobility: 0.92 cm^2 V^{-1} s^{-1} in G2 versus 0.56 cm^2 V^{-1} s^{-1} in G1 films. The resistivity of Cu-doped TiN_xO_y films at room temperature was 202 ± 4 $\mu\Omega$ cm, which is about 10 times higher than that of pure TiN but over 3 orders of magnitude smaller than in similar composition-undoped TiN_xO_y films obtained by other groups. The effective resistivity of the surface-segregated copper-doped TiN_xO_y layer was estimated to be 52.6 $\mu\Omega$ cm. The Un-doped TiN_xO_y films had a room-temperature resistivity of 484 ± 8 $\mu\Omega$ cm, and their $R(T)$ behavior was drastically different from the Cu-doped ones: the former showed a steadily decreasing trend at approximately $-1.88T^{0.6}$ + 604 $\mu\Omega$ cm, while the latter revealed quantum interference effects at temperatures below 50 K and a semimetallic linear character above 50 K, similar to 2D thin copper reported by others. The TCR of Cu-doped TiN_xO_y measured 150 ppm $°C^{-1}$, which was 6 times lower than that of films grown without intentional copper doping and almost 20 times smaller than that for single-crystal TiN. The medium range resistivity and low TCR of the surface-segregated Cu-doped TiN_xO_y make this material an attractive choice for the improved matching resistors in RF analog circuits operating at varied temperatures. This process should be compatible with the standard Si CMOS damascene copper metallization BEOL process of SoC chips and, therefore, may be promising for future-integrated circuits.

AUTHOR INFORMATION

Corresponding Author

Filipp A. Baron − *Kirensky Institute of Physics, Federal Research Center KSC SB RAS, Krasnoyarsk 660036, Russia;* orcid.org/0000-0002-7313-7994; Email: baron@iph.krasn.ru, filippbaron@mail.ru

Authors

Yurii L. Mikhlin − *Institute of Chemistry and Chemical Technology, Federal Research Center KSC SB RAS, Krasnoyarsk 660036, Russia*

Maxim S. Molokeev − *Kirensky Institute of Physics, Federal Research Center KSC SB RAS, Krasnoyarsk 660036, Russia; Siberian Federal University, Krasnoyarsk 660041, Russia;* orcid.org/0000-0002-8297-0945

Mikhail V. Rautskiy − *Kirensky Institute of Physics, Federal Research Center KSC SB RAS, Krasnoyarsk 660036, Russia*

Ivan A. Tarasov − *Kirensky Institute of Physics, Federal Research Center KSC SB RAS, Krasnoyarsk 660036, Russia*

Mikhail N. Volochaev − *Kirensky Institute of Physics, Federal Research Center KSC SB RAS, Krasnoyarsk 660036, Russia; Reshetnev Siberian State University of Science and Technology, Krasnoyarsk 660037, Russia*

Lev V. Shanidze − *Kirensky Institute of Physics, Federal Research Center KSC SB RAS, Krasnoyarsk 660036, Russia*

Anna V. Lukyanenko − *Kirensky Institute of Physics, Federal Research Center KSC SB RAS, Krasnoyarsk 660036, Russia; Siberian Federal University, Krasnoyarsk 660041, Russia*

Tatiana E. Smolyarova − *Kirensky Institute of Physics, Federal Research Center KSC SB RAS, Krasnoyarsk 660036, Russia; Siberian Federal University, Krasnoyarsk 660041, Russia*

Stepan O. Konovalov − *Reshetnev Siberian State University of Science and Technology, Krasnoyarsk 660037, Russia*

https://doi.org/10.1021/acsami.1c08036
ACS Appl. Mater. Interfaces 2021, 13, 32531−32541

Fyodor V. Zelenov − *Reshetnev Siberian State University of Science and Technology, Krasnoyarsk 660037, Russia*
Anton S. Tarasov − *Kirensky Institute of Physics, Federal Research Center KSC SB RAS, Krasnoyarsk 660036, Russia; Siberian Federal University, Krasnoyarsk 660041, Russia*
Nikita V. Volkov − *Kirensky Institute of Physics, Federal Research Center KSC SB RAS, Krasnoyarsk 660036, Russia*

Complete contact information is available at: https://pubs.acs.org/10.1021/acsami.1c08036

Author Contributions

The manuscript was written through contributions of all authors. All authors have given approval to the final version of the manuscript.

Funding

This research was funded by the RFBR, Krasnoyarsk Territory and Krasnoyarsk Regional Fund of Science (project code 20-42-240013) and by the grant of the Government of the Russian Federation for Creation of World Tier Laboratories (contract no. 075-15-2019-1886).

Notes

The authors declare no competing financial interest.

■ ACKNOWLEDGMENTS

The authors would like to thank the Krasnoyarsk Territorial Shared Resource Center, Krasnoyarsk Scientific Center and Russian Academy of Sciences and Krasnoyarsk Regional Center of Research Equipment of the Federal Research Center "Krasnoyarsk Science Center SB RAS" for providing access to TEM, XPS, AFM, and XRD equipment and assistance with the measurements.

■ ABBREVIATIONS

SoC, system-on-chip
TCR, temperature coefficient of resistance
BEOL, back-end-of-the-line
IC, integrated circuit
FGCD, forming gas-mediated copper doping
Un-doped, unintentionally doped
ALD, atomic layer deposition
AFM, atomic force microscopy
XPS, X-ray photoemission spectroscopy
XRD, X-ray diffraction analysis
TEM, transmission electron microscopy
G1, unintentionally doped TiN_xO_y grown without forming gas ALD chamber pre-treatment
G2, intentionally copper-doped TiN_xO_y grown with forming gas ALD chamber pre-treatment

■ REFERENCES

(1) Scholten, C. A. System-on-a-Chip: What Industry Needs to Do. *Solid State Technol.* **2000**, *43*, 121−123.
(2) Cuong, N. D.; Kim, D.-J.; Kang, B.-D.; Yoon, S. G. Structural and Electrical Properties of TiN_xO_y Thin-Film Resistors for 30 dB Applications of π-type Attenuator. *J. Electrochem. Soc.* **2006**, *153*, G856−G859.
(3) Musschoot, J.; Xie, Q.; Deduytsche, D.; Van der Berghe, S.; Van Meirhaeghe, R. L.; Detavernier, C. Atomic Layer Deposition of Titanium Nitride from TDMAT Precursor. *Microelectron. Eng.* **2009**, *86*, 72−77.
(4) Gadre, K. S.; Alford, T. L.; Mayer, J. W. Use of TiN(O)/Ti as an Effective Intermediate Stress Buffer and Diffusion Barrier for Cu/parylene-n Interconnects. *Appl. Phys. Letts* **2001**, *79*, 3260−3262.
(5) Li, J.; Mayer, J. W.; Colgan, E. G. Oxidation and Protection in Copper and Copper Alloy Thin Films. *J. Appl. Phys.* **1991**, *70*, 2820−2827.
(6) Iwashita, S.; Aoyama, S.; Nasu, M.; Shimomura, K.; Noro, N.; Hasegawa, T.; Akasaka, Y.; Miyashita, K. Periodic Oxidation for Fabricating Titanium Oxynitride Thin Films Via Atomic Layer Deposition. *J. Vac. Sci. Technol., A* **2016**, *34*, 01A145-1−01A145-6.
(7) Asahi, R.; Morikawa, T.; Ohwaki, T.; Aoki, K.; Taga, Y. Visible-Light Photocatalysis in Nitrogen-Doped Titanium Oxides. *Science* **2001**, *293*, 269−271.
(8) Martinez-Ferrero, E.; Sakatani, Y.; Boissi, C.; Grosso, D.; Fuertes, A.; Fraxedas, J.; Sanchez, C. Nanostructured Titanium Oxynitride Porousthin Films as Efficient Visible-Active Photocatalysts. *Adv. Funct. Mater.* **2007**, *17*, 3348−3354.
(9) Lazarov, M.; Raths, P.; Metzger, H.; Spirkl, W. Optical Constants and Film Density of TiN_xO_y Solar Selective Absorbers. *J. Appl. Phys.* **1995**, *77*, 2133−2137.
(10) Rizzo, A.; Signore, M. A.; Tapfer, L.; Piscopiello, E.; Cappello, A.; Bemporad, E.; Sebastiani, M. Graded Selective Coatings Based on Zirconium and Titanium Oxynitride. *J. Phys. D: Appl. Phys.* **2009**, *42*, 115406 (10pp).
(11) Yang, X.; Lin, Y.; Liu, J.; Liu, W.; Bi, Q.; Song, X.; Kang, J.; Xu, F.; Xu, L.; Hedhili, M. N.; Baran, D.; Zhang, X.; Anthopoulos, T. D.; De Wolf, S. A Highly Conductive Titanium Oxynitride Electron-Selective Contact for Efficient Photovoltaic Devices. *Adv. Mater.* **2020**, *32*, 2002608.
(12) Zhang, X.; Yu, Y.; Jiang, D.; Jiao, Y.; Wu, Y.; Peng, Z.; Zhou, J.; Wu, J.; Dong, Z. Synthesis and Characterization of a Bi-functional Hydroxyapatite/Cu-doped TiO_2 Composite Coating. *Ceram. Int.* **2019**, *45*, 6693−6701.
(13) Alotaibi, A. M.; Williamson, B. A. D.; Sathasivam, S.; Kafizas, A.; Alqahtani, M.; Sotelo-Vazquez, C.; Buckeridge, J.; Wu, J.; Nair, S. P.; Scanlon, D. O.; Parkin, I. P. Enhanced Photocatalytic and Antibacterial Ability of Cu-Doped Anatase TiO_2 Thin Films: Theory and Experiment. *ACS Appl. Mater. Interfaces* **2020**, *12*, 15348−15361.
(14) Mathew, S.; Ganguly, P.; Rhatigan, S.; Kumaravel, V.; Byrne, C.; Hinder, S. J.; Bartlett, J.; Nolan, M.; Pillai, S. Cu-Doped TiO_2: Visible Light Assisted Photocatalytic Antimicrobial Activity. *Appl. Sci.* **2018**, *8*, 2067.
(15) Ilkhechi, N. N.; Kaleji, B. K.; Salahi, E.; Hosseinabadi, N. Comparison of Optical and Structural Properties of Cu Doped and Cu/Zr co-Doped TiO2 Nanopowders Calcined at Various Temperatures. *J. Sol-Gel Sci. Technol.* **2015**, *74*, 765−773.
(16) López, R.; Gómez, R.; Llanos, M. E. Photophysical and Photocatalytic Properties of Nanosized Copper-Doped Titania Sol−Gel Catalysts. *Catal. Today* **2009**, *148*, 103−108.
(17) Navas, J.; Sánchez-Coronilla, A.; Aguilar, T.; Hernández, N. C.; de los Santos, D. M.; Sánchez-Marquez, J.; Zorrilla, D.; Fernández-Lorenzo, C.; Alcántara, R.; Martín-Calleja, J. Experimental and Theoretical Study of the Electronic Properties of Cu-doped Anatase TiO_2. *Phys. Chem. Chem. Phys.* **2014**, *16*, 3835−3845.
(18) Myung, H. S.; Lee, H. M.; Shaginyan, L. R.; Han, J. G. Microstructure and Mechanical Properties of Cu Doped TiN Superhard Nanocomposite Coatings. *Surf. Coat. Technol.* **2003**, *163-164*, 591−596.
(19) Olowolafe, J. O.; Li, J.; Mayer, J. W.; Colgan, E. G. Effects of Oxygen in TiNx on the Diffusion of Cu in Cu/TiN/Al and Cu/TiNx/Si Structures. *Appl. Phys. Lett.* **1991**, *58*, 469−471.
(20) Johansson, B. O.; Sundgren, J.-E.; Greene, J. E.; Rockett, A.; Barnett, S. A. Growth and Properties of Single Crystal TiN Films Deposited by Reactive Magnetron Sputtering. *J. Vac. Sci. Technol., A* **1985**, *3*, 303−307.
(21) Abd El-Fattah, H. A.; El-Mahallawi, I. S.; Shazly, M. H.; Khalifa, W. A. Optical Properties and Microstructure of TiN_xO_y and TiN Thin Films Before and After Annealing at Different Conditions. *Coatings* **2019**, *9*, 22. (15pp)
(22) Braic, L.; Vasilantonakis, N.; Mihai, A.; Villar Garcia, I. J.; Fearn, S.; Zou, B.; McN, N.; Doiron, A. B.; Oulton, R. F.; Maier, S. A.; Zayats, A. V.; Petrov, P. K. Titanium Oxynitride Thin Films With

Tunable Double Epsilon-Near-Zero Behavior for Nanophotonic Applications. *ACS Appl. Mater. Interfaces* **2017**, *9*, 29857−29862.
(23) Vaz, F.; Martin, N.; Fenker, M. *Metallic Oxynitride Thin Films by Reactive Sputtering and Related Deposition Methods: Processes, Properties and Applications*; Bentham Science Publishers: Sharjah, U.A.E, 2013.
(24) Chappé, J.-M.; Martin, N.; Lintymer, J.; Sthal, F.; Terwagne, G.; Takadoum, J. Titanium Oxynitride Thin Films Sputter Deposited by the Reactive Gas Pulsing Process. *Appl. Surf. Sci.* **2007**, *253*, 5312−5316.
(25) Mucha, N. R.; Som, J.; Shaji, S.; Fialkova, S.; Apte, P. R.; Balasubramanian, B.; Shield, J. E.; Anderson, M.; Kumar, D. Electrical and Optical Properties of Titanium Oxynitride Thin Films. *J. Mater. Sci.* **2020**, *55*, 5123−5134.
(26) Krylov, I.; Zoubenko, E.; Weinfeld, K.; Kauffmann, Y.; Xu, X.; Ritter, D.; Eizenberg, M. Obtaining Low Resistivity (∼100 $\mu\Omega$ cm) TiN Films by Plasma Enhanced Atomic Layer Deposition Using a Metalorganic Precursor. *J. Vac. Sci.Technol., A* **2018**, *36*, 051505-1−051505-10.
(27) Kot, M.; Henkel, K.; Das, C.; Brizzi, S.; Kärkkänen, I.; Schneidewind, J.; Naumann, F.; Gargouri, H.; Schmeißer, D. Analysis of Titanium Species in Titanium Oxynitride Films Prepared by Plasma Enhanced Atomic Layer Deposition. *Surf. Coat. Technol.* **2017**, *324*, 586−593.
(28) Gu, J. J.; Liu, Y. Q.; Wu, Y. Q.; Colby, R.; Gordon, R. G.; Ye, P. D. First Experimental Demonstration of Gate-all-around IIIV MOSFETs by Top-down Approach. *IEDM Tech. Dig.* **2011**, 769−772.
(29) Li, Y.; Liang, T.; Wang, R.; He, B.; Gong, Y.; Wang, H. Encapsulation of Fe_3O_4 between Copper Nanorod and Thin TiO_2 Film by ALD for Lithium-Ion Capacitors. *ACS Appl. Mater. Interfaces* **2019**, *11*, 19115−19122.
(30) Mao, Z.; Wang, H.; Chao, D.; Wang, R.; He, B.; Gong, Y.; Fan, H. J. Al2O3-Assisted Confinement Synthesis of Oxide/Carbon Hollow Composite Nanofibers and Application in Metal-Ion Capacitors. *Small* **2020**, *16*, 2001950 (9pp).
(31) Tarasov, I. A.; Visotin, M. A.; Aleksandrovsky, A. S.; Kosyrev, N. N.; Yakovlev, I. A.; Molokeev, M. S.; Lukyanenko, A. V.; Krylov, A. S.; Fedorov, A. S.; Varnakov, S. N.; Ovchinnikov, S. G. Si/Fe Flux Ratio Influence on Growth and Physical Properties of Polycrystalline β-$FeSi_2$ Thin Films on Si(100) Surface. *J. Magn. Magn. Mater.* **2017**, *440*, 144.
(32) Forouhi, A. R.; Bloomer, I. Optical Dispersion Relations for Amorphous Semiconductors and Amorphous Dielectrics. *Phys. Rev. B* **1986**, *34*, 7018−7026.
(33) der Pauw, L. V. A Method of Measuring Specific Resistivity and Hall Effect of Discs of Arbitrary Shape. *Philips Res. Rep.* **1991**, *13*, 1−9.
(34) Bui, H. V.; Kovalgin, A. Y.; Aarnink, A. A. I.; Wolters, R. A. M. Hot-Wire Generated Atomic Hydrogen and its Impact on Thermal ALD in TiCl4/NH3System. *ECS J. Solid State Sci.Technol.* **2013**, *2*, P149−P155.
(35) Ritala, M.; Leskelä, M.; Dekker, J.-P.; Mutsaers, C.; Soininen, P. J.; Skarp, J. Perfectly Conformal TiN and Al_2O_3 Films Deposited by Atomic Layer Deposition. *Chem. Vap. Deposition* **1999**, *5*, 7 (9pp).
(36) Satta, A.; Schuhmacher, J.; Whelan, C. M.; Vandervorst, W.; Brongersma, S. H.; Beyer, G. P.; Maex, K.; Vantomme, A.; Viitanen, M. M.; Brongersma, H. H.; Besling, W. F. A. Growth Mechanism and Continuity of Atomic Layer Deposited TiN Films on Thermal SiO_2. *J. Appl. Phys.* **2002**, *92*, 7641−7646.
(37) Ahn, C. H.; Cho, S. G.; Lee, H. J.; Park, K. H.; Jeong, S. H. Characteristics of TiN Thin Films Grown by ALD Using $TiCl_4$ and NH_3. *Met. Mater. Int.* **2001**, *7*, 621−625.
(38) Kim, B.-Y.; Lee, S.-H.; Park, S.-G.; Oh, K.-Y.; Song, J.; Kim, D.-H. Comparison Study for TiN Films Deposited from Different Method: Chemical Vapor Deposition and Atomic Layer Deposition. *Mater. Res. Soc. Symp. Proc.* **2001**, *672*, O7.8.1−O7.8.6.
(39) Kim, J.; Hong, H.; Ghosh, S.; Oh, K.-Y.; Lee, C. Physical Properties of Highly Conformal TiN Thin Films Grown by Atomic Layer Deposition. *Jpn. J. Appl. Phys.* **2003**, *42*, 1375−1379.
(40) Krylov, I.; Qi, Y.; Korchnoy, V.; Weinfeld, K.; Eizenberg, M.; Yalon, E. Zero Temperature Coefficient of Resistance in Back-end-of-the-line Compatible Titanium Aluminum Nitride Films by Atomic Layer Deposition. *Appl. Phys. Lett.* **2020**, *117*, 041902.
(41) Xiang, J.; Ding, Y.; Du, L.; Li, J.; Wang, W.; Zhao, C. Growth Mechanism of Atomic-layer-deposited TiAlC Metal Gate Based on $TiCl_4$ and TMA Precursors. *Chin. Phys. B* **2016**, *25*, 037308-1−037308-4.
(42) Assaud, L.; Pitzschel, K.; Hanbücken, M.; Santinacci, L. Highly-Conformal TiN Thin Films Grown by Thermal and Plasma-Enhanced Atomic Layer Deposition. *ECS J. Solid State Sci. Technol.* **2014**, *3*, P253−P258.
(43) Jaeger, D.; Patscheider, J. A Complete and Self-consistent Evaluation of XPS Spectra of TiN. *J. Electron Spectrosc. Relat. Phenom.* **2012**, *185*, 523−534.
(44) Grosso, S.; Latu-Romain, L.; Berthome, G.; Renou, G.; Coz, T. L.; Mantel, M. T. Titanium and Titanium Nitride Thin Films Grown by DC Reactive Magnetron Sputtering Physical Vapor Deposition in a Continuous Mode on Stainless Steel Wires: Chemical, Morphological and Structural Investigations. *Surf. Coat. Technol.* **2017**, *324*, 318−327.
(45) Hyde, G. K.; McCullen, S. D.; Jeon, S.; Stewart, S. M.; Jeon, H.; Loboa, E. G.; Parsons, G. N. Atomic Layer Deposition and Biocompatibility of Titanium Nitride Nano-coatings on Cellulose Fiber Substrates. *Biomed. Mater.* **2009**, *4*, No. 025001, (10pp).
(46) Gao, X.-H.; Guo, Z.-M.; Geng, Q.-F.; Ma, P.-J.; Wang, A.-Q.; Liu, G. Enhanced Optical Properties of TiN-based Spectrally Selective Solar Absorbers Deposited at a High Substrate Temperature. *Sol. Energy Mater. Sol. Cells* **2017**, *163*, 91−97.
(47) White, N.; Campbell, A. L.; Grant, J. T.; Pachter, R.; Eyink, K.; Jakubiak, R.; Martinez, G.; Ramana, C. V. Surface/interface Analysis and Optical Properties of RF Sputter-deposited Nanocrystalline Titanium Nitride Thin Films. *Appl. Surf. Sci.* **2014**, *292*, 74−85.
(48) Lu, F.-H.; Chen, H.-Y. XPS Analyses of TiN Films on Cu Substrates After Annealing in the Controlled Atmosphere. *Thin Solid Films* **1999**, *355-356*, 374−379.
(49) Brager, A. An X-ray Examination of Titanium Nitride III. *Acta Physicochim. (USSR)* **1939**, *9*, 617−632.
(50) Bruker AXS *TOPAS V4: General Profile and Structure Analysis Software for Powder Diffraction Data. − User's Manual*; Bruker AXS: Karlsruhe, Germany, 2008.
(51) Uhm, J.; Jeon, H. TiN Diffusion Barrier Grown by Atomic Layer Deposition Method for Cu Metallization. *Jpn. J. Appl. Phys.* **2001**, *40*, 4657−4660.
(52) Martin, N.; Besnard, A.; Sthal, F.; Takadoum, J. The Reactive Gas Pulsing Process for Tuneable Properties of Sputter Deposited Titanium Oxide, Nitride and Oxynitride Coatings. *Int. J. Mater. Prod. Technol.* **2010**, *39*, 159−177.
(53) Schnabel, V.; Spolenak, R.; Doebeli, M.; Galinski, H. Structural Color Sensors with Thermal Memory: Measuring Functional Properties of Ti-Based Nitrides by Eye. *Adv. Opt. Mater.* **2018**, *6*, 1800656 (5pp).
(54) Pflüger, J.; Fink, J.; Weber, W.; Bohnen, K. P.; Crecelius, G. Dielectric Properties of TiC_x, TiN_x, VC_x, and VN_x from 1.5 to 40 eV Determined by Electron-energy-loss Spectroscopy. *Phys. Rev. B* **1984**, *30*, 1155−1163.
(55) Chen, F.; Wang, S.-W.; Yu, L.; Chen, X.; Lu, W. Control of optical properties of TiN_xO_y Films and Application for High Performance Solar Selective Absorbing Coatings. *Opt. Mater. Express* **2014**, *4*, 1833−1847.
(56) Chappé, J.-M.; Nicolas, M. *Gradual Evolution of the Properties in Titanium Oxynitride Thin Films, Metallic Oxynitride Thin Films by Reactive Sputtering and Related Deposition Methods*; BENTHAM SCIENCE PUBLISHERS 2013, 113−132.
(57) Solovan, M. N.; Brus, V. V.; Maistruk, E. V.; Maryanchuk, P. D. Electrical and Optical Properties of TiN Thin Films. *Inorg. Mater.* **2014**, *50*, 40−45.

https://doi.org/10.1021/acsami.1c08036
ACS Appl. Mater. Interfaces 2021, 13, 32531−32541

(58) Von Seefeld, H.; Cheung, N. W.; Maenpaa, M.; Nicolet, M.-A. Investigation of Titanium-Nitride Layers for Solar-Cell Contacts. *IEEE Trans. Electron Dev.* **1980**, *27*, 873−876.
(59) Patsalas, P.; Logothetidis, S. Optical, electronic, and transport properties of nanocrystalline titanium nitride thin films. *J. Appl. Phys.* **2001**, *90*, 4725−4734.
(60) Yang, X.; Liu, W.; De Bastiani, M.; Allen, T.; Kang, J.; Xu, H.; Aydin, E.; Xu, L.; Bi, Q.; Dang, H.; AlHabshi, E.; Kotsovos, K.; AlSaggaf, A.; Gereige, I.; Wan, Y.; Peng, J.; Samundsett, C.; Cuevas, A.; De WolfDual, S. Dual-Function Electron-Conductive, Hole-Blocking Titanium Nitride Contacts for Efficient Silicon Solar Cells. *Joule* **2019**, *3*, 1314−1327.
(61) Narayan, J.; Tiwari, P.; Chen, X.; Singh, J.; Chowdhury, R.; Zheleva, T. Epitaxial Growth of TiN Films on (100) Silicon Substrates by Laser Physical Vapor Deposition. *Appl. Phys. Lett.* **1992**, *61*, 1290−1292.
(62) Roy, M.; Mucha, N. R.; Ponnam, R. G.; Jaipan, P.; Scott-Emuakpor, O.; Yarmolenko, S.; Majumdar, A. K.; Kumar, D. Quantum Interference Effects in Titanium Nitride Films at Low Temperatures. *Thin Solid Films* **2019**, *681*, 1−5.
(63) Lee, P. A.; Ramakrishnan, T. V. Disordered Electronic Systems. *Rev. Mod. Phys.* **1985**, *57*, 287−337.
(64) Barone, C.; Romeo, F.; Pagano, S.; Attanasio, C.; Carapella, G.; Cirillo, C.; Galdi, A.; Grimaldi, G.; Guarino, A.; Leo, A.; Nigro, A.; Sabatino, P. Nonequilibrium Fluctuations as a Distinctive Feature of Weak Localization. *Sci. Rep.* **2015**, *5*, 1−11.
(65) Barone, C.; Rotzinger, H.; Mauro, C.; Dorer, D.; Münzberg, J.; Ustinov, A. V.; Pagano, S. Kondo-like Transport and Magnetic Field Effect of Charge Carrier Fluctuations in Granular Aluminum Oxide Thin Films. *Sci. Rep.* **2018**, *8*, 13892 (10pp).
(66) da Silva, A. F.; Sernelius, B. E.; de Souza, J. P.; Boudinov, H.; Zheng, H.; Sarachik, M. P. Impurity Resistivity of the Double-donor System Si:P,Bi. *Phys. Rev. B* **1999**, *60*, 15824−15828.
(67) Sernelius, B. E. Temperature-dependent Resistivity of Heavily Doped Silicon and Germanium. *Phys. Rev. B* **1990**, *41*, 3060−3068.
(68) Havemann, R. H.; Antonelli, A.; Arendt, G. K.; Danek, M.; McKerrow, A. J.; Weinberg, R. S. Copper BEOL Solutions for Advanced Memory. *Solid State Technol.* **2009**, *52*, 10−15.
(69) Kriz, J.; Angelkort, C.; Czekalla, M.; Huth, S.; Meinhold, D.; Pohl, A.; Schulte, S.; Thamm, A.; Wallace, S. Overview of Dual Damascene Integration Schemes in Cu BEOL Integration. *Microelectron. Eng.* **2008**, *85*, 2128−2132.

https://doi.org/10.1021/acsami.1c08036
ACS Appl. Mater. Interfaces 2021, 13, 32531−32541